REVISTA MATÉRIA V.29 N.1
ISSN 1517-7076 articles e20230240, 2024

Influence of tensile strength on the load bearing capacity of tall reinforced masonry walls

Tiago Montanha Padilha[1], Guilherme Aris Parsekian[1], Joel Araújo do Nascimento Neto[2]

[1]Universidade Federal de São Carlos, Programa de Pós-Graduação em Engenharia Civil. São Carlos, SP, Brasil.
[2]Universidade Federal do Rio Grande do Norte, Departamento de Engenharia Civil e Ambiental. Natal, RN, Brasil.
e-mail: engciv_tiago@yahoo.com.br, parsekian@ufscar.br, joel.neto@ufrn.br

ABSTRACT

Rupture by geometric instability is a common characteristic in slender walls. Codes for the design of slender walls use the slenderness ratio (λ) as a parameter for which their methods are valid. The Brazilian standard has a specific method for the design of highly slender walls with $\lambda > 30$ that does not take into account the tensile strength of the masonry. To evaluate the behavior of high slenderness walls and the sensitivity to tensile strength, a finite element model was developed using Abaqus to simulate three experiments from the literature. The results proved the ability of the modeling to represent the behavior of slender walls with 20% error for the out-of-plane displacements and vertical load bearing capacity. It was concluded that the post buckling behavior of the walls is sensitive to tensile strength and negligible for determining the critical buckling load.

Keywords: Loading-bearing masonry; buckling; finite element modeling.

1. INTRODUCTION

1.1. Buckling criteria

A slender wall under axial forces may rupture due to material failure or buckling, characterized by sudden and progressive lateral displacement with one side of the wall compressed and the other tensioned. The masonry's tensile strength is low compared to its compressive strength. The possibility of buckling is greater the taller and thinner the wall. Maximum limits for the design of slender masonry are imposed by standards and codes using the slenderness ratio (λ) as a parameter. These maximum values vary in each country. For the Italian, Eurocode 6, Australian and Brazilian standards [1–4], reinforced masonry walls could be designed and built with slenderness ratios smaller than the respective values 20, 27, 36 and 30. After updates, Eurocode 6 and the Australian standard [2, 4] started to adopt the maximum limit slenderness ratio equal to $\lambda = 40$. The Brazilian standard [5], as well as the Canadian standard [6], started to indicate the slenderness ratio equal to $\lambda = 30$, not as a design limiter, but as an indicator parameter to consider different requirements in the calculation procedure. To this end, a series of requirements presented in Annex C of ABNT NBR 16868-1:2020 [5] was established for cases where $\lambda > 30$. However, the literature has indicated that for $\lambda = 40$ the rupture occurs by compression [7, 8] and that the transition from compression rupture mode to buckling rupture occurs at $\lambda = 60$ [8]. To investigate the influence of slenderness and load eccentricity on the bearing capacity of slender walls, YOKEL *et al.* [9] performed experiments and applications of analytical methods, with reinforced and unreinforced masonry. YOKEL *et al.* [9] identified that the end support conditions of the wall, parameter also verified more recently in PETTIT *et al.* [10], the elasticity modulus of the masonry, the shape of the bending moment diagram, and the geometric properties of the section, such as the second moment area are variables not considered in the normative criteria, but that significantly affect the masonry behavior. YOKEL *et al.* [9] applied concepts from the formulation developed in MACGREGOR *et al.* [11] to verify buckling of reinforced concrete columns in masonry walls. In this formulation, 40% of the product between the elasticity modulus and the second moment of area of the uncracked reinforced section was taken into account for simplified consideration of damage by cracking and loss of stiffness. The authors [9] also found that for unreinforced masonry only 28.5% of the uncracked stiffness can be considered. By assuming a linear distribution of normal stresses, considering total compression of the section for eccentricities (e) smaller than 1/6 of the thickness (t), YOKEL [12] published an analytical solution,

Corresponding Author: Tiago Montanha Padilha Received on 14/08/2023 Accepted on 07/12/2023

DOI: https://doi.org/10.1590/1517-7076-RMAT-2023-0240

Equation 1, to determine the critical load (P_{cr}) and the consequent lateral instability of a full section prismatic element with no tensile strength.

$$P_{cr} = 0.285 \cdot \left(\frac{9}{4} \cdot \frac{E \cdot L \cdot u^3}{H^2} \right) \tag{1}$$

In Equation 1, E is the elasticity modulus, I is the second moment of area, L is the length of the cross section, H is the height of the wall, u is the distance between the axis of load application and the most compressed edge. The deduction of Equation 1 can be found in YOKEL [12]. With the results of the 68-wall experiment, HATZINIKOLAS *et al.* [13] developed an analytical study including geometric imperfections, with initial eccentricities and initial deformed configuration, to determine the static equilibrium of slender walls. Two formulations resulted from their analysis, Equation 2 considering with no tensile strength of masonry and Equation 3 considering the bond strength between unit and mortar.

$$P_{cr} = 8\pi^2 \left(\frac{1}{2} - \frac{e}{t} \right)^3 \frac{E \cdot I}{H^2} \tag{2}$$

$$P_{cr} = \frac{\pi^2 E}{12H^2} \left[\left(1 - \frac{2e}{t} \right) t + \tau \right]^3 \tag{3}$$

Where t is the wall thickness, e is the eccentricity of vertical load application and τ is the width of the tensile stress diagram, i.e., the distance between the neutral line and the tensile bond stress between block and mortar.

The Brazilian, Canadian and American standards [5, 6, 14] allow the design of high walls with high slenderness. In Brazilian standards (ABNT NBR 16868-1:2020 [5]) the critical load value can calculate by Equation 4 for reinforced masonry with no tensile strength, considering the net area of the section.

$$P_{cr} = \frac{\pi^2 (E \cdot I)_{ef}}{H^2 (1 + 0.5\beta_d)\gamma_m} \tag{4}$$

Where β_d is the ratio between the bending moments of the permanent vertical load and the total, it is included in the expression to account creep effects. The term $(EI)_{ef}$ in Equation 4 and Equation 5 represents an effective stiffness to account the wall cracking. The bearing capacity of the wall reducing coefficient of the masonry is given by γ_m. Further information can be found in the respective standards.

A similar formulation, Equation 5, is presented in CSA [6] to determine the critical load in masonry with no tensile strength and net area.

$$P_{cr} = \frac{\pi^2 \cdot \phi_e \cdot (E \cdot I)_{ef}}{(kH)^2 \cdot (1 + 0.5\beta_d)} \tag{5}$$

Where ϕ_e is the resistance factor for the stiffness and k is the effective height coefficient, which depends on the end support conditions of the wall.

The critical load according to MSJC [14] is determined by Equation 6, where r is the radius of gyration of the section, which also takes into account the net area and the no tensile strength of the masonry.

$$P_{cr} = \frac{\pi^2 \cdot E \cdot I}{H^2} \left(1 - 0.577 \frac{e}{r} \right)^3 \tag{6}$$

The contribution of tensile strength can be significant to accurately determine the stress due vertical action over masonry at failure, especially in walls with high slenderness ratio and eccentric vertical loads with $e \geq t/10$ in unreinforced walls [15] and also in reinforced walls subject to buckling [16]. The Brazilian, Canadian and American standards [5, 6, 14] present different theoretical values for tensile strength and different criteria for its determination, as can be seen in Table 1.

The standards formulations mentioned above [5, 6, 14] do not take into account any contribution of tensile strength in the bearing capacity of the wall to buckling. To analyze the influence of tensile strength on the

Table 1: Characteristic values for flexural tensile strength, [5, 6, 14].

STANDARDS AND ADDITIONAL CHARACTERISTICS		MASONRY TENSILE STRENGTH FTK (MPA)			MORTAR
		ORTHOGONAL TO THE COURSE	PARALLEL TO THE COURSE	TYPE	$f_{c,m}$ (MPa)
MSJC:2022 [14]	Ungrouted	0.33	0.65	N	5.2
	Grouted	1.09	1.03		
	Ungrouted	0.43	0.86	M and S	12.4 and 17.2
	Grouted	1.12	1.38		
NBR 16868:2020 [5]		0.10	0.20	–	1.5 up to 3.4
		0.20	0.40		3.5 up to 7.0
		0.25	0.50		Over 7.0
CSA S304:2014 [6]	Solid clay brick	0.50	1.00	N	–
		0.65	1.30	S	
	Hollow clay brick	0.20	0.35	N	
		0.30	0.55	S	
	Calcium silicate brick	0.25	0.55	N	
		0.30	0.80	S	
	Concrete blocks and bricks	0.30	0.45	N	
		0.40	0.55	S	
	Hollow blocks and bricks, grouted	0.50	0.55	N	
		0.65	0.85	S	

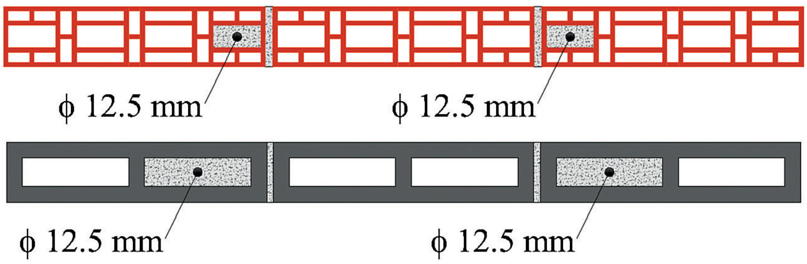

Figure 1: Reinforcement position [17].

bearing capacity and behavior of slender walls, a 3D macromodel was developed to simulate three experiments reported in the literature [13, 17, 18]. These three studies used for validation will now be discussed in the following section.

1.2. Studies investigated

1.2.1. Tests by PARSEKIAN *et al.* [17]

To investigate slenderness limits in reinforced and unreinforced masonry wall designs with clay and concrete blocks, PARSEKIAN *et al.* [17] conducted twelve experiments of walls with thickness of 9.0 cm and slenderness ratio equal to 31. The walls with a length of three blocks (L = 1.20 m) in each course were hinged at the base and top of the wall, while their sides remained free. At the top of the wall was placed a strip of Shore A 60 elastomer with the same dimensions of the cross section and thickness equal to 1.0 cm and at the bottom support another strip with horizontal dimensions equal to 120 cm × 4.4 cm and height equal to 3.0 cm. The load was applied uniformly at the top to the wall. The lateral displacements were measured at four heights, and the largest displacement before rupture was read at half height (H = 1.40 m) of the wall. In the reinforced walls, two bars with ϕ = 12.5 mm positioned in the center line of the section were used as shown in Figure 1. A comparative study of procedures of international standards (American, Australian, British, Canadian and European) was also carried out to evaluate the recommendations of the Brazilian standard [3].

According to the authors, in walls with clay blocks, the Canadian standard [6] was the only one that presented an adequate value, 40% lower than the experimental compressive stress. The other standards, including the Brazilian [3], presented greater differences, some values exceeded up to 4 times the experimental failure stress. The authors pointed out that in the design procedures all the calculation for determining the bearing capacity of the walls should be done in the net area of the wall and not in the gross area as is usual, because it would result in inaccuracy of the results. They further pointed out that consideration of the PΔ effect provides accurate results. From the experimental results, they indicated that walls with slenderness greater than 30 are very unstable, this conclusion agrees with the design limitations by slenderness. The authors' conclusion converges with SAHLIN [19] which indicates that in masonry walls with h/t > 30 the possibility of failure by buckling is predominant.

1.2.2. Tests by ACI-SEASC [18]

The American Concrete Institute (ACI) organized a committee to develop normative recommendations for the design of slender concrete panels and structural masonry. This committee conducted experiments with 30 walls, 9 of them with dimensions 4' × 24' feet (equivalent to 1.22 × 7.31 meters) built with concrete blocks with three different thicknesses t = 9–5/8" (equivalent to 24.45 cm), with t = 7–5/8" (equivalent to 19.37 cm) and with thickness t = 5–5/8" (equivalent to 14.29 cm). The panels were fully grouted and reinforced with five #4 bars (ϕ = 12.5 mm) positioned on the center line of the section as shown in Figure 2.

The panels were connected to the frame with hinged supports. Half of a 101.6 mm diameter pipe, cut in the longitudinal axis, was welded under the base plate. The horizontal dimension of the plate has the same values as the transverse section of the wall and a thickness equal to 12.7 mm. A 6" × 6" × 3/8" metal ledger angle (equivalent to 15.24 × 15.24 × 0.95 centimeters) was tied on one side, at the top, and along the entire length of the panel to apply the eccentric load of the actuator. The vertical load, invariable, was provided with steel drums loaded with water, while the lateral load, incremental, was applied by means of an air bag between the frame

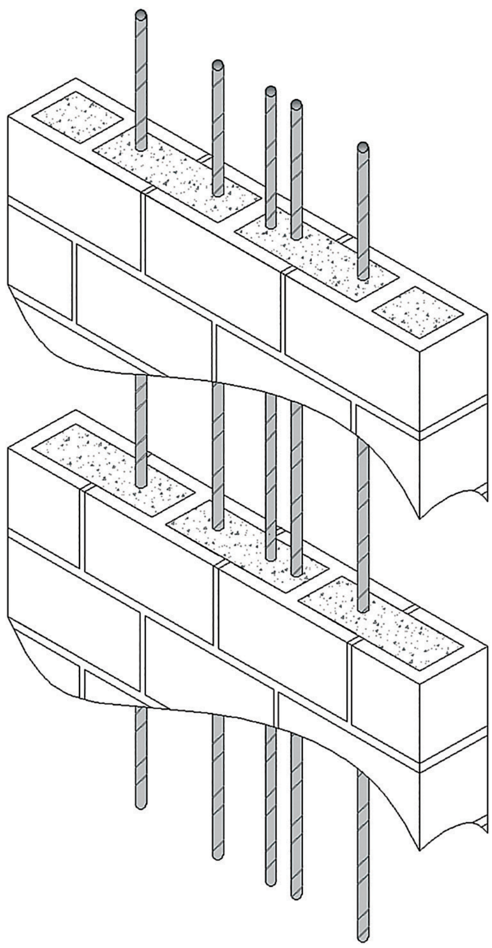

Figure 2: Reinforcement position [18].

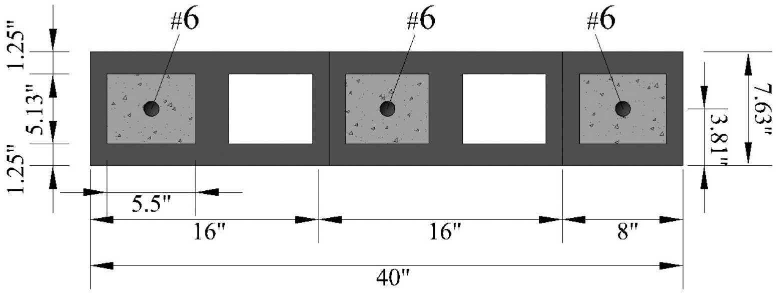

Figure 3: Reinforcement position [13].

and the panel. With the results, the committee analyzed the effects of slenderness, PΔ effects, and the influence of the bending moment due to the eccentricity of the vertical load and the horizontal load, and developed and presented several examples of the procedure for designing slender panels.

In the tests, they identified that the initial cracks occurred in the mortar. A 30% ratio was determined between the lateral service load and the self-weight of the 6” wall (t = 14.3 mm). By relating the lateral deflection at this service load to the free height of the concrete block wall, a relationship H/D = 115.2 was determined. The authors [18] considered that, for one-story buildings, this ratio is acceptable to limit service displacements. In the Brazilian standard [5], the maximum service displacement is limited by the ratio H/250.

1.2.3. Tests by HATZINIKOLAS *et al.* [13]

The walls tested by HATZINIKOLAS *et al.* [13] were constructed with two and a half blocks, L = 4” (1.02 m), in each course and with thickness equal to t = 7-5/8” (19.37 cm) and variable height that resulted in slenderness ratios between $13.8 \leq \lambda \leq 24.2$. The walls were grouted in the first and last course to avoid damage from stress concentration and to uniform the load distribution. The tests included both reinforced and unreinforced walls. Vertical bars #3, #6 and #9 (10 mm, 20 mm and 30 mm) positioned according to Figure 3 were used for reinforcement. The boundary conditions included concentric and eccentric vertical loading with hinged support ends and with free sides.

A metal plate with the same dimensions of the masonry cross section and thickness equal to 63.5 mm was used at the upper end of the wall for load application and at the lower end to support the wall. A metallic roller with diameter equal to 60 mm tied in the center line of the lower metallic plate was used to provide a pinned connection. With their results they found that the theoretical elastic modulus (E) (using Hooke’s Law) of masonry and the $E = 1000 \cdot f_{pk}$ showed values 16% and 33% higher than the experimental E and proposed that $750 \cdot f_{pk}$ would be more appropriate for design development, a ratio that resulted in a value 0.2% lower than their test results. In addition, they proposed the formulations for calculating the critical load already presented in this paper (Equation 2 and Equation 3).

2. FINITE ELEMENT MODELING

To investigate the influence of masonry tensile strength on the behavior of slender walls, the 3D macro-modeling technique was used where the block, mortar and grout are grouped into a single assemblage. The prism strength was assumed to be the strength of the single masonry assemblage, divided into two regions when grouted and another when not grouted, containing a specific prism strength for each. Only the properties of the prism, assumed to be masonry, are considered. The isolated properties of the individual elements that assemble the masonry are not used and their individual failures or interaction are not analyzed. For this analysis, the tensile strength (f_{tk}) of the masonry was the parameter investigated. Four values of f_{tk} equal to 0.1 MPa, 0.2 MPa, 0.5 MPa, and 1.0 MPa were used. These values are based on bending tests of prisms lying with concrete blocks found in [20] and [21] and also correspond to the range of values presented in the American, Brazilian and Canadian standards [14, 5, 6]. This analysis was divided into two stages. In the first stage the same tensile strength was used for the ungrouted prism and the grouted prism. In the second stage, the value f_{tk} = 0.1 MPa was maintained for the ungrouted prism and alternated for the grouted prism. The analysis of the variation of f_{tk} was performed on the model that simulates the CPI and CPII walls tests performed by PARSEKIAN *et al.* [17], where CPI and CPII are acronym used in the original study that meaning test specimen number 1 and number 2, respectively.

The model was validated by the C2 wall experiment found in HATZINIKOLAS *et al.* [13], where C2 is the same acronym used by the authors [13], and also by the thinnest and tallest panels tested by the American committee [18] numbered from 4 to 9. Both experiments were simulated with two high strength metal plates were associated with the masonry, one for the load application at the top of the wall and the other to support the base. The reinforcement, consisting of vertical bars, was adhered to the grout by the Embedded command. To model the masonry, the actuator and the steel support, solid type finite elements were used, with linear polynomial function and reduced numerical integration, with nomenclature C3D8R, present in the Abaqus computational package. All models were processed with geometric non-linearity activated. For the steel bars T3D2 elements were used. The Newton Rapshon numerical method available in the Static General analysis was used. A mesh with dimensions equal to 25 x 25 millimeters was adopted to define the approximate size of the finite elements.

2.1. Materials constitutive model

The constitutive model was defined in Concrete Damage Plasticity (CDP), originally formulated to represent the behavior of quasi-brittle materials (i.e., concrete), with plasticity parameters that have been used by other researchers [7, 22–26] in simulations of prisms and structural masonry with results that proved to be adequate. The same values for CDP defined by BOLHASSANI *et al.* [22] were used which, in turn, are very close to those defined by [7, 23–25]. Table 2 contains the values adopted for each CDP parameter.

The compressive behavior was defined as bilinear up to the peak stress, the intermediate point being equivalent to 40% of the maximum stress. The post-peak compressive behavior was defined as linear up to the ultimate stress, corresponding to the ultimate strain ε_u = 3,5‰. The value of the ultimate stress was determined by the formulation proposed by GUO [27]. The simplified elastoplastic constitutive model was used for the steel bars. Only the linear elastic behavior was defined in the metal plates.

Poisson coefficients $\nu = 0.2$ for masonry and $\nu = 0.3$ for steel were adopted for all simulations. The geometry and values of the mechanical properties were adopted according to the test data. Theoretical values were adopted for the properties not reported in the publications, such as the tensile strength of the prism. The Table 3 contains the values used in the simulations.

Table 2: CDP Parameters.

DILATION ANGLE	ECCENTRICITY	FB0/FC0	K	VISCOSITY
34	0.1	1.16	0.6667	0.001

Table 3: Constitutive properties of the prisms used in the simulations.

AUTHOR	UNGROUTED PRISM				GROUTED PRISM			
	Compression (MPa)		Tensile (MPa)		Compression (MPa)		Tensile (MPa)	
	Stress	Strain	Stress	Strain	Stress	Strain	Stress	Strain
PARSEKIAN *et al.* [17]	E = 4120 MPa				E = 5366.7 MPa			
	4.944	0	0.100*	0	6.44	0	0.100*	0
	12.36	0.0030	0.101*	0.00035	16.10	0.0030	0.101*	0.00035
	11.282	0.0035	–	–	14.695	0.0035	–	–
HATZINIKOLAS *et al.* [13]	E = 3960 MPa				E = 3329 MPa			
	5.544	0	0.200	0	4.66	0	0.400	0
	13.860	0.0030	0.201	0.00035	11.65	0.0030	0.401	0.00035
	12.651	0.0035	–	–	10.279	0.0035	–	–
ACI-SEASC [18]	Grouted Prism. t = 14.3 cm				Grouted Prism. t = 19.4 cm			
	E = 7320 MPa				E = 5963.3 MPa			
	8.784	0	0,800	0	7.156	0	1.200	0
	21.960	0.0030	0,801	0.0035	17.890	0.0030	1.201	0.0035
	20.054	0.0035	–	–	16.337	0.0035	–	–

* The f_{tk} value used in the model validation.

Table 4: Mechanical properties of the reinforcing steel bars.

AUTHOR	E (MPA)	STRESS (MPA)	STRAIN
PARSEKIAN *et al.* [17]	210 000	501.19	0
	–	545.4	0.0074
HATZINIKOLAS *et al.* [13]	191 000	410	0

For the metal plates of the load actuator and the wall base support, hypothetical values were assumed, to consider an infinitely rigid and resistant plate, with high strength $f_s = 10^9$ MPa and elasticity modulus $E_s = 2 \times 10^{11}$ MPa. The reinforcing steel bars properties are shown in the Table 4.

Elastic properties were set E = 60 MPa and ν = 0,5 for the elastomers in the simulation of the tests by PARSEKIAN *et al.* [17]. The value of ν = 0,5 was made possible by using the hybrid type C3D8RH finite element for the elastomer. The finite element represents an elastic and isotropic material and has volumetric compression properties.

2.2. Boundary conditions and loading

On the face of the top plate in all simulations where the loading was considered concentric, the points were coupled in such a way that they resulted in a minimum eccentricity equal to e = t/10 because of constructive imperfections.

In the simulation of the experiment by PARSEKIAN *et al.* [17], a reference point was coupled, with kinematic coupling constraint, to the nodes on the top surface of the wall top plate and another on the underside of the elastomer support plate. This procedure causes each plate to have the same movements or constraints as the reference point. In this way, the base reference point was restricted to all degrees of freedom, i.e., fixed, making the rotation of the base of the wall dependent only on the loading and the elastomer deformation capacity, as in the experiment. At the top reference point, vertical displacement and out-of-plane rotation of the wall were not restricted. Also, a symmetry condition was set on one side of the wall to mirror the results, i.e., only half of the wall was modeled. To obtain the post-peak behavior of the simulation, displacements were imposed instead of forces. It was noted that the deformed wall configuration in [17], showed horizontal displacements at the top and bottom of the wall. Initially, a horizontal displacement equal to $U3_{TOP}$ = 18 mm and vertical displacement of U2 = –10 mm was imposed at the top reference point. At the top edge of the base elastomer a displacement of $U3_{BASE}$ = 5 mm was imposed. This set of imposed displacements were applied with automatic increments of varying sizes. The proportion of each increment significantly affects the second order effects and the final results evaluated, such as the out-of-plane wall displacement and the maximum load. Thus, the imposed displacement set was calibrated to U2 = –4.8 mm, $U3_{TOP}$ = 17 mm and $U3_{BASE}$ = 5 mm.

In the HATZINIKOLAS *et al.* [13] test simulation the plate surface nodes were coupled in a way that resulted in a load eccentricity equal to e = t / 11.87 and in the RP-Top all translations were restricted, rotation out of the wall plane was kept free and a vertical displacement was imposed equal to U2 = –12.1 mm.

In the ACI-SEASC [18] panel simulations, a reference point (RP-1) was coupled to the nodes of the top surface angle of the wall top face. At this RP-1 point, all motions except vertical displacement and rotation out of the plane of the wall were constrained. Another RP-Base reference point was attached to the center edge of the roller surface, all motions were constrained at the points on this edge. Unlike the previous simulations, in this one the lateral load *vs* out-of-plane displacement curve of the wall at mid-height that led the steel to yield was evaluated. A constant vertical load with 4.67 kN/m was applied to the angle of panels 6, 7, 8 and 9 and another with 12.55 kN/m was applied to panels 4 and 5.

In the model, a concentrated vertical load was applied at RP-1 with equivalent value of the final resultant with an increase of 20%, being, therefore, P1 = –6.832 kN and P2 = –18.361 kN. Preliminary models with the application of the load with exact values from the experiment did not achieve the same experimental values for the steel yielding displacements. The value of lateral pressure to reach the yielding of steel in panels 4 and 5 was 3.59 kN/m^2, 3.40 kN/m^2 in panel 6, and 2.20 kN/m^2 in panels 7 and 9, and 1.82 kN/m^2 in panel 8. A reference point (RP-wind) was created attached to the entire surface of one of the panel faces, with distributing coupling constraint, from the base to the height where the angle was positioned. The applied pressure on each panel increased by +20% was transformed into a concentrated horizontal load and applied to the RP-wind. The boundary conditions of the simulations for each test are shown in the Figure 4.

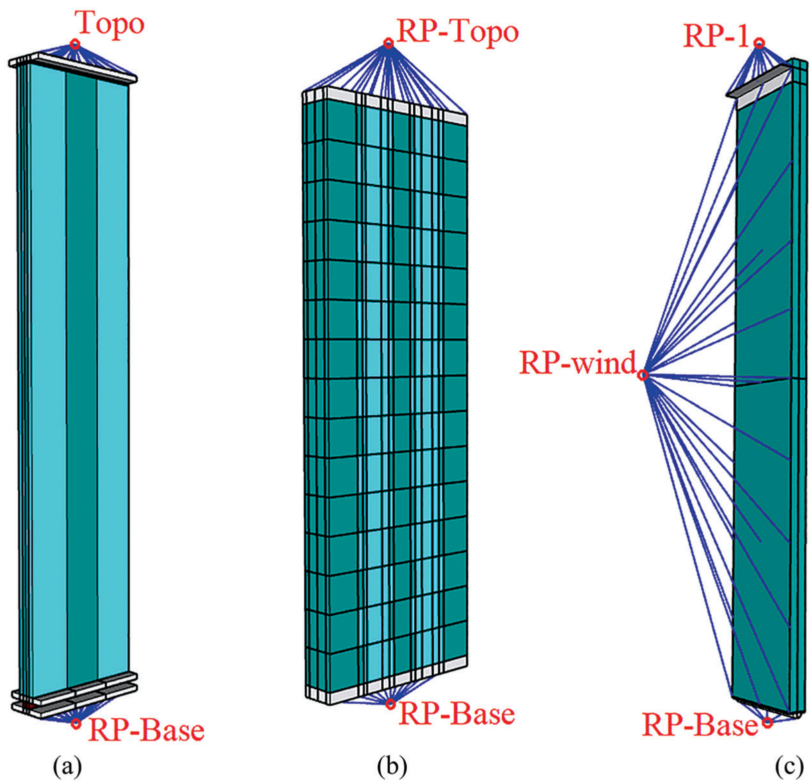

Figure 4: Boundary conditions simulations: (a) PARSEKIAN *et al*. [17], (b) HATZINIKOLAS *et al.* [13], (c) ACI-SEASC [18].

3. RESULTS

3.1. Model validation results

The readings of lateral displacements along the wall height at maximum load in HATZINIKOLAS *et al.* [13] and PARSEKIAN *et al*. [17] were compared between simulations and tests. While in the simulations of the ACI-SEASC [18] tests, the displacements at mid-height of the wall and the resultant of the horizontal load at the steel yielding were compared.

3.1.1. Simulation results of the test by PARSEKIAN *et al.* [17]

Due to the remaining differences in the top and bottom wall displacements in the results of PARSEKIAN *et al*. [17], a normalization of the deformations was performed. A linear function was determined, between the first and the last reading point, for each deformation. The differences in displacements between each curve and its linear function were plotted in a new, normalized deformed configuration, Figure 5. The mean normalized displacement at mid-height of the wall in the experiment resulted in $\Delta_{average}$ = 12.88 mm, and Δ = 13.37 mm in the computational model, a difference of +2.2%. The values of the displacements at each height are shown in Table 5.

The maximum load from the PARSEKIAN *et al*. [17] simulation, P_{max} = 201.76 kN was compared to the average failure load P_u = 214.22 kN of the CPI and CPII walls, resulting in a difference of –5.7%. The maximum lateral displacement (Δ) occurs at mid-height of the wall in both the model, with Δ = 24.62 mm, and in the experiment $\Delta_{average}$ = 24.09 mm.

3.1.2. Simulation results of the test by HATZINIKOLAS *et al.* [13]

In the simulation of HATZINIKOLAS *et al.* [13], the difference between the maximum model load (P_{max} = 1108 kN) and the experimental failure load (P_u = 1401 kN) resulted in –20.9%. The lateral displacement at 1.70 m height of the wall in the calibrated model resulted in Δ_{model} = 1.03 mm, a difference of +18% compared to the experimental displacement equal to Δ_{exp} = 0.88 mm at the same height, Figure 6. The values of the displacements at each height of both the experiment wall C2 and the computational model are shown in Figure 6. The values of the displacements at each height for both the C2 wall from the experiment by HATZINIKOLAS *et al.* [13] and the computational model are shown in Table 6.

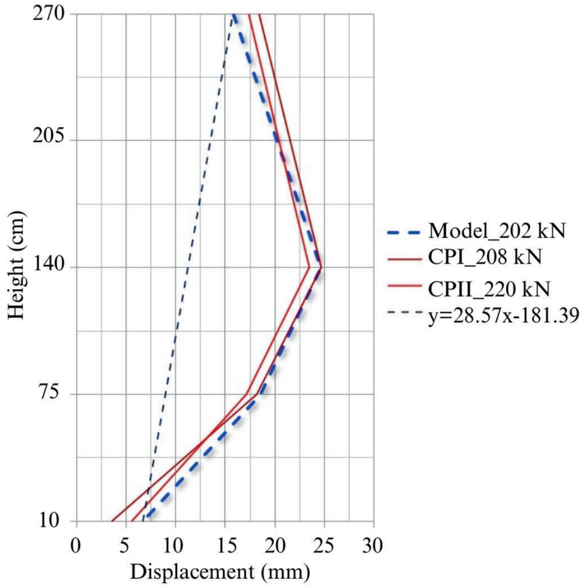

(a) Original profile.

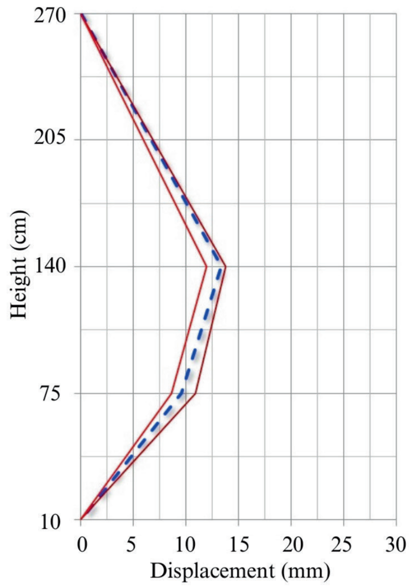

(b) Normalized profile.

Figure 5: Displacements at ultimate loading and failure: (a) original, (b) normalized, PARSEKIAN *et al.* [17].

Table 5: Displacement results, model and test in PARSEKIAN *et al*. [17].

	HEIGHT (CM)	DISPLACEMENT (CM)			DISPLACEMENT (CM)			DISPLACEMENT (CM)	
		ORIGINAL	NORMALIZED		ORIGINAL	NORMALIZED		ORIGINAL	NORMALIZED
CPI	270	18.4	0.0	CPII	17.4	0.0	Model	15.80	0.0
	140	24.7	13.8		23.5	12.0		24.62	13.37
	75	18.1	10.9		17.1	8.6		18.58	9.61
	10	3.6	0.0		5.5	0.0		6.70	0.0

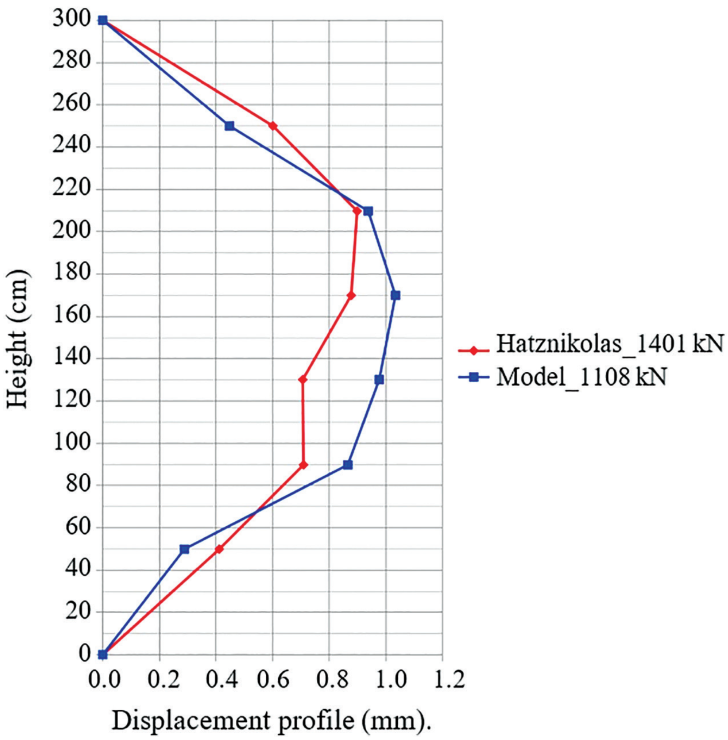

Figure 6: Deformations at ultimate (model) and rupture (test) loading, [13].

Table 6: Displacement results, model and test in HATZINIKOLAS *et al.* [13].

HEIGHT (CM)	DISPLACEMENT (MM)	
	C2	MODEL
250	0.60	0.45
210	0.90	0.94
170	0.88	1.03
130	0.71	0.98
90	0.71	0.86
50	0.41	0.29

3.1.3. Simulation results of the test by ACI-SEASC [18]

The graph in Figure 7 contains the results obtained for panels 4, 5 and 6 from ACI-SEASC [18]. The simulation of panels 4 and 5 with side loading –1.5% of the average experimental loading, resulted in a displacement difference equal to –0.5%. The simulation of panel 6 with load 2.1% greater than the load in the experiment, resulted in a displacement difference of –0.6%. Note in the graph, Figure 7, that the largest difference occurs at the 50 mm displacement where the model loads, 20 kN, are approximately 21% greater than the average experimental load, 16.5 kN.

The results for panels 7, 8 and 9 are shown in the graph in Figure 8. For panels 7 and 9 the difference in loading between model and experiment and their respective displacements resulted in $P_{mod}/P_{exp} = -3.9\%$ and $\%\Delta = -0.2\%$. For panel 8, the differences in percent resulted in $P_{mod}/P_{exp} = -0.2\%$ and $\%\Delta = -2.89\%$.

With the computational modeling, it was possible to simulate the tests by PARSEKIAN *et al.* [17] and HATZINIKOLAS *et al.* [13] with walls only subjected to centered vertical loads, the former of which resulted in failure due to buckling and the latter due to material failure. With this model, it was also possible to reproduce the ACI-SEASC tests [18] with vertically and laterally loaded walls whose failure occurred due to material failure. The results of this study of the influence of tensile strength on the load-bearing capacity of the wall subjected to buckling are shown in the following section, using the model developed to simulate the PARSEKIAN *et al.* [17] tests.

3.2. Tensile strength variance analysis results

To analyze the influence of tensile strength on the load-bearing capacity of walls subject to buckling, only the model developed to simulate the tests of PARSEKIAN *et al.* [17] was used. In the first stage of the analysis, the lower tensile strength values (0.1 MPa and 0.2 MPa) resulted in maximum loads closer to the experimental average (214 kN), in PARSEKIAN *et al.* [17], as shown in Figure 9. For these values, the maximum load varied from 201.76 kN to 250 kN, an increase equal to 23.9%. For the higher tensile strength values (0.5 MPa and 1.0 MPa) the difference in maximum load varied from 276.5 kN to 279.5 kN an increase of 1.1%, these values, however, are further away from the experimental mean value.

It was noted that the small variation from 0.1 MPa to 0.2 MPa resulted in a greater difference in the maximum load. For the larger variation from 0.5 MPa to 1.0 MPa, the difference resulted smaller. Therefore, the tensile stress spectrum distributed in the vertical axis of the walls, was analyzed. In the spectrum, it was identified that the tensile limit stresses, with gray coloring in Figure 10, in the models with 0.1 MPa and 0.2 MPa were reached before the maximum load. It is assumed that damage and, consequently, cracks arise when the limit stresses are exceeded. Thus, it was identified that the walls cracked by tensile and continued to resist higher loads. In the other two models (with 0.5 MPa and 1.0 MPa) the cracking started after the decline of the maximum load, in these models the cracking started in the grouted blocks unlike the previous models (0.1 MPa and 0.2 MPa) that cracked, initially, in the ungrouted blocks. Therefore, in walls that present buckling, the lower the tensile strength the more significant is the change in behavior, including the pattern of crack initiation.

For the second step of the sensitivity analysis, the tensile strength value was set equal to 0.1 MPa, because the model with this value resulted in a maximum load closer to the average value of the experimental load. For the grouted prism, values between 0.1 MPa and 0.5 MPa were tested. The results in Figure 11 indicate that for the grouted prism the appropriate tensile strength is 0.2 MPa.

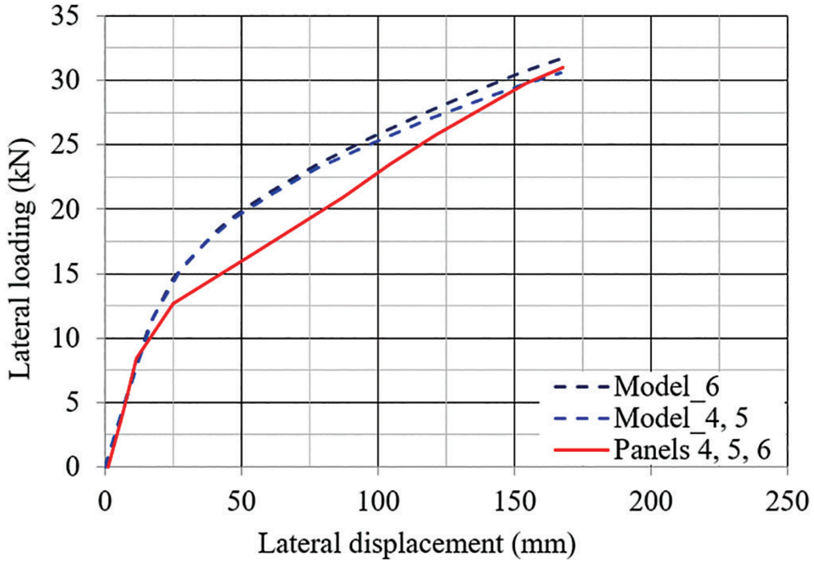

Figure 7: Load vs Displacement graph, model and test, panels 4, 5 e 6 in ACI-SEASC [18].

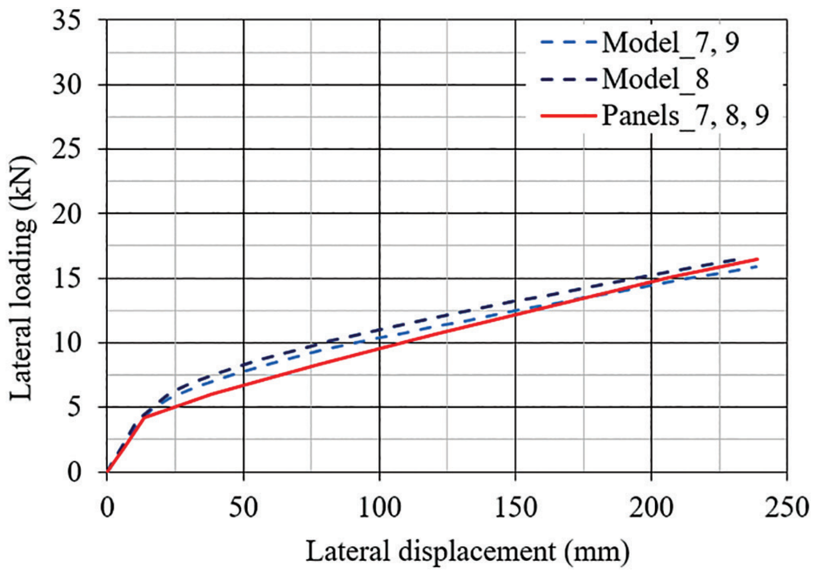

Figure 8: Load vs Displacement graph, model and test, panels 7, 8 e 9 in ACI-SEASC [18].

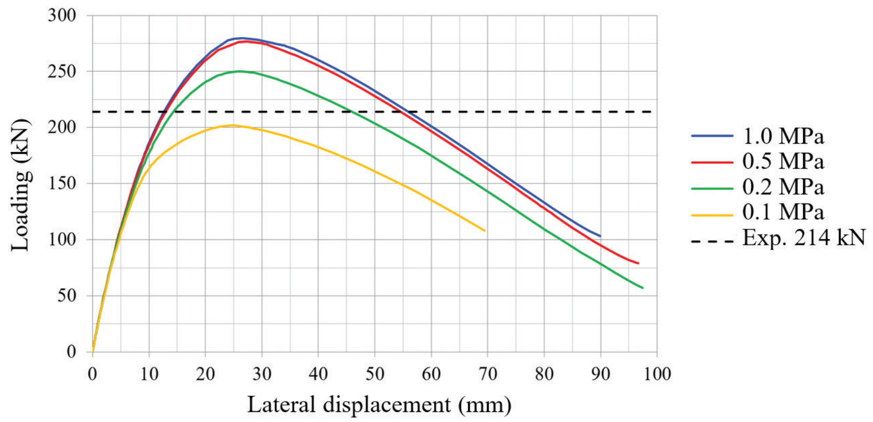

Figure 9: Lateral displacement vs Loading, equal f_{tk} to grouted and ungrouted prism.

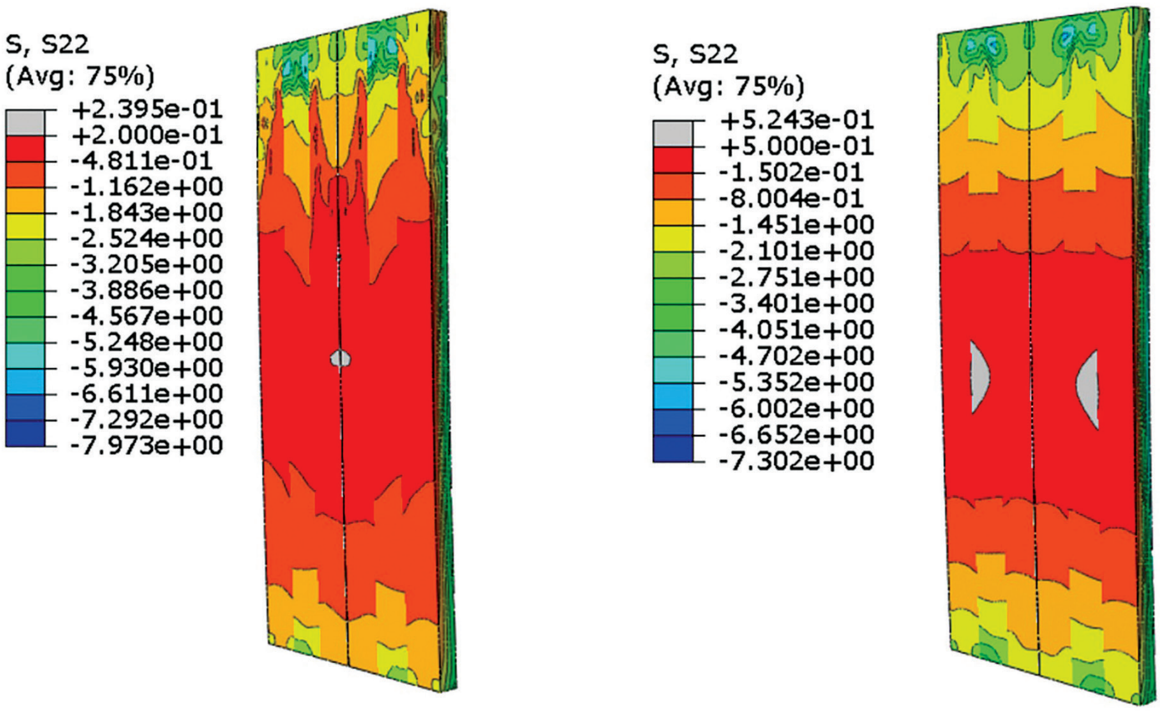

(a) Model with f_{tk} = 0.2 MPa (b) Model with f_{tk} = 0.5 MPa

Figure 10: Tensile stress spectrum, sensitivity analysis.

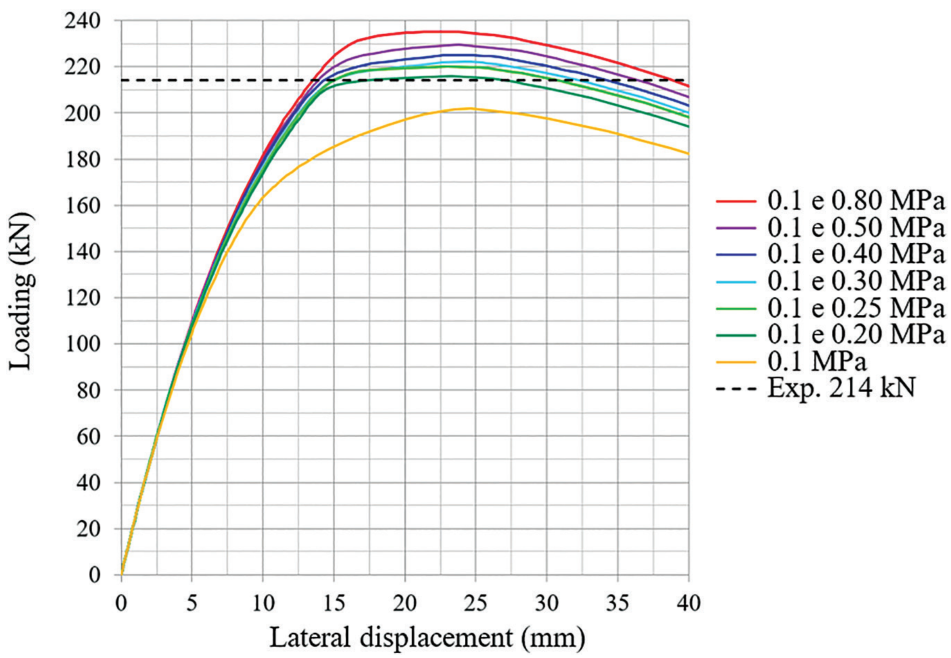

Figure 11: Graph Lateral displacement vs Loading, different f_{tk} to grouted and ungrouted prism.

The model (Model_216 kN), with these tensile strength values, resulted in maximum load equal to 215.8 kN, maximum displacement equal to Δ = 23.3 mm, Figure 12 (a), and normalized equal to Δ = 12.19 mm, Figure 12 (b), a difference of –3.5%. Compared to the previous validation model (Model_202 kN), the differences remained +/– 6.0% in the displacements, while for the maximum load there was an improvement in the accuracy of the new model, with –5.8% previously, changed to +0.7%.

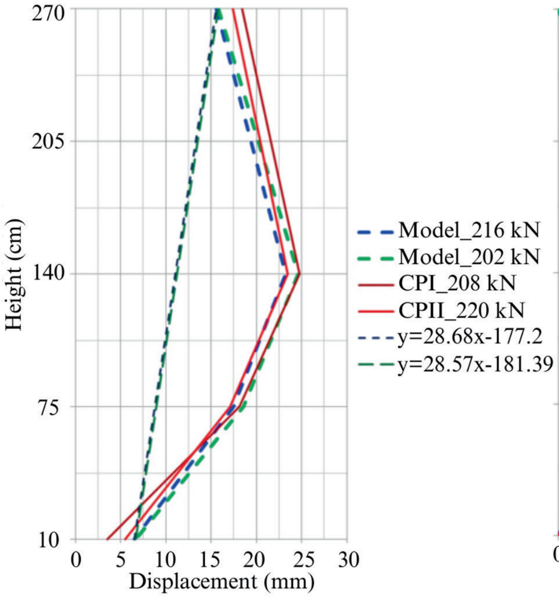

(a) Original profile.

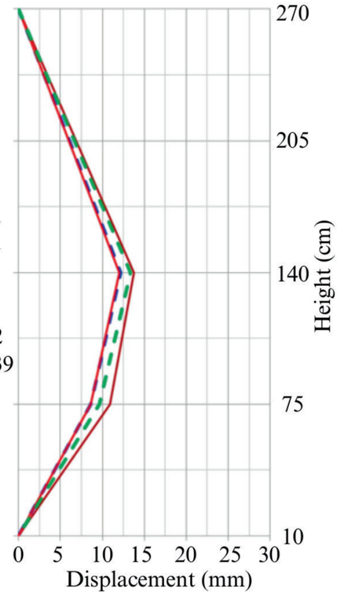

(b) Normalized profile.

Figure 12: Displacement profile with calibrated f_{tk} to grouted and ungrouted prism.

4. CONCLUSIONS

In this analysis of the slender wall's behavior in which the walls with slenderness ratios λ = 15.87, λ = 31, λ = 38 and λ = 51.2 under concentric, eccentric and combined vertical and horizontal loading, orthogonal to the panel plane, were simulated, it is concluded that:

The 3D macromodel used in this research, with properties of the grouted prism in the grouted region of the wall and the hollow prism in the ungrouted region, homogeneous material and CDP model for the material behavior was able to approximately reproduce the behavior of slender walls under various loading modes.

The use of the elastomer to enable small rotations in the experiment was also verified in the computational model. However, in the experiment, the low value of the transverse modulus of the elastomer may have affected the translations.

The influence of tensile strength on walls that rupture due to geometric instability is minimal before buckling. The walls crack in tension and continue to resist higher loads. In these cases, it was concluded that the lower the tensile strength, the more significant is the change in behavior, including the pattern of crack initiation, and thus, the lower the bearing capacity of the wall.

5. BIBLIOGRAPHY

[1] MINISTERO DELLE INFRASTRUTTURE E DEI TRASPORTI, *Norme Tecniche per le Costruzioni: Supplemento ordinário nº 8*, Roma, NTC, 2018.

[2] EUROPEAN COMMITTEE FOR STANDARDIZATION, *CEN 1992-1-1 Eurocode 2: design of concrete structures: Part 1-1: General rules and rules for buildings*, Brussels, Eurocode, 2005.

[3] ASSOCIAÇÃO BRASILEIRA DE NORMAS TÉCNICAS, *ABNT NBR 15961-1: Alvenaria Estrutural: blocos de concreto: Parte 1: Projeto*, Rio de Janeiro, ABNT, 2011.

[4] STANDARDS ASSOCIATION OF AUSTRALIA, *Masonry Structures AS 3700*, Sydney, Standards Association Of Australia, 2018.

[5] ASSOCIAÇÃO BRASILEIRA DE NORMAS TÉCNICAS, *ABNT NBR 16868-1: Alvenaria Estrutural: Parte 1: Projeto*, Rio de Janeiro, ABNT, 2020.

[6] CANADIAN STANDARDS ASSOCIATION, *S304-14: Design of Masonry Structures*, Ontario, CSA, 2014.

[7] AHMED, A., ISKANDER, G., BOGOSLAVOV, M., *et al*. "Examining the mode of failure of slender concrete block walls", In: *Canadian Masonry Symposium*, Montreal, Canada, 2021.

[8] ISFELD, A.C., HAGEL, M.D., SHRIVE, N.G. "Finite element analysis of hollow concrete block masonry walls", In: *North American Masonry Conference*, Salt Lake City, Utah, 2019.

[9] YOKEL, F.Y., MATHEY, R.G., DIKKERS, R.D., Compressive strength of slender concrete masonry walls, Washington, DC, US National Bureau of Standards, Building Science Series, 1970.

[10] PETTIT, C., MOHSIN, E., CRUZ-NOGUEZ, C., *et al*., "Experimental testing of slender load-bearing masonry walls with realistic support conditions", *Canadian Journal of Civil Engineering*, v. 39, pp. 95–108, 2020.

[11] MACCREGOR, J.G., BREEN, J.E., PFRANG, E.O., "Design of slender concrete columns", *ACI Journal*, v. 67, pp. 6–28, 1970.

[12] YOKEL, F.Y., "Stability and load capacity of members with no tensile strength", *Journal of the Structural Division*, v. 97, n. 7, pp. 1913–1926, 1971. doi: http://dx.doi.org/10.1061/JSDEAG.0002954.

[13] HATZINIKOLAS, M., LONGWORTH, J., WARWARUK, J., *Concrete Masonry Walls: Structural Engineering Report No. 70*, Edmonton, Canada, University of Alberta, 1978.

[14] MASONRY STANDARDS JOINT COMMITTEE, *Build Code Requirements for Masonry Structures – ACI 530-02 / ASCE 5-02 / TMS 402-02*, Colorado, MSJC, 2022.

[15] SANDOVAL, C., ROCA, P., "Empirical equations for the assessment of the load-bearing capacity of brick masonry walls", *Construction & Building Materials*, v. 44, pp. 427–439, 2013. doi: http://dx.doi.org/10.1016/j.conbuildmat.2013.03.025.

[16] DONÀ, M., TECCHIO, G., PORTO, F., "Verification of second-order effects in slender reinforced masonry walls", *Materials and Structures*, v. 51, n. 3, pp. 1–15, 2018. doi: http://dx.doi.org/10.1617/s11527-018-1196-x.

[17] PARSEKIAN, G.A., CORRÊA, M.R.S., LOPES, G.M., *et al*., "Estudo teórico e experimental de paredes esbeltas de alvenaria estrutural", *Ambiente Construído*, v. 16, n. 4, pp. 197–213, 2016. doi: http://dx.doi.org/10.1590/s1678-86212016000400114.

[18] AMERICAN CONCRETE INSTITUTE, STRUCTURAL ENGINEERS ASSOCIATION OF SOUTHERN CALIFORNIA, *Task Committee on Slender Walls: Test Report on Slender Walls*, Los Angeles, ACI-SEASC, 1982.

[19] SAHLIN, S., *Structural Masonry*, New Jersey, Prentice Hall, 1971.

[20] MATOS, P.R.D., SCHANKOSKI, R.A., PILAR, R., *et al*., "Using ready-mixed mortars in concrete block structural masonry", *Ambiente Construído*, v. 20, n. 3, pp. 431–449, 2020. doi: http://dx.doi.org/10.1590/s1678-86212020000300438.

[21] PARSEKIAN, G.A., "*Tecnologia de produção de alvenaria estrutural protendida*", D.Sc. Thesis, Polytechnic School of the University of São Paulo, São Paulo, Brazil, 2002.

[22] BOLHASSANI, M., HAMID, A.A., LAU, A.C.W., *et al*., "Simplified micro modeling of partially grouted masonry assemblages", *Construction & Building Materials*, v. 83, pp. 159–173, 2015. doi: http://dx.doi.org/10.1016/j.conbuildmat.2015.03.021.

[23] ISFELD, A.C., MÜLLER, A. L., HAGEL, M., *et al*., "Finite element modelling of concrete block walls under axial and out of plane loading", In: *International Masonry Conference*, Milan, Italy, 2018.

[24] MEDEIROS, W.A., "*Pórticos em concreto pré-moldado preenchidos com alvenaria participante*", M.Sc. Thesis, PPGECiv/UFSCar, São Carlos, Brazil, 2018.

[25] SANTOS, C.F.R., ALVARENGA, R.C.S.S., RIBEIRO, J.C.L., *et al*., "Numerical and experimental evaluation of masonry prisms by finite element method", *Revista IBRACON de Estruturas e Materiais*, v. 10, n. 2, pp. 477–508, 2017. doi: http://dx.doi.org/10.1590/s1983-41952017000200010.

[26] MISIR, I.S., YUCEL, G., "Numerical model calibration and a parametric study based on the out-of-plane drift capacity of stone masonry walls", *Buildings*, v. 13, n. 2, pp. 437, 2023. doi: http://dx.doi.org/10.3390/buildings13020437.

[27] GUO, Z., *Principles of reinforced concrete*, Oxford, Butterworth-Heinemann, 2014.